Supplementary Information

Raman Fingerprints of Atomically Precise Graphene Nanoribbons

I. A. Verzhbitskiy,[1,†] Marzio De Corato,[2, 3] Alice Ruini,[2, 3] Elisa Molinari,[2, 3] Akimitsu Narita,[4] Yunbin Hu,[4] Matthias Georg Schwab,[4, ‡] M. Bruna,[5] D. Yoon, [5] S. Milana,[5] Xinliang Feng,[6] Klaus Müllen,[4] Andrea C. Ferrari, [5] Cinzia Casiraghi,[1, 7,*] and Deborah Prezzi[3,*]

[1] *Physics Department, Free University Berlin, Germany*

[2] *Dept. of Physics, Mathematics, and Informatics, University of Modena and Reggio Emilia, Modena, Italy*

[3] *Nanoscience Institute of CNR, S3 Center, Modena, Italy*

[4] *Max Planck Institute for Polymer Research, Mainz, Germany*

[5] *Cambridge Graphene Centre, University of Cambridge, Cambridge, CB3 OFA, UK*

[6] *Center for Advancing Electronics Dresden (cfaed) & Department of Chemistry and Food Chemistry, Technische Universitaet Dresden, Germany*

[7] *School of Chemistry, University of Manchester, UK*

[†] Present address: Physics Department, National University of Singapore, 117542, Singapore

[‡] Present address: BASF SE, Carl-Bosch-Straße 38, 67056 Ludwigshafen, Germany

* Corresponding authors: (DP) deborah.prezzi@nano.cnr.it; (CC) cinzia.casiraghi@manchester.ac.uk

Table of Contents

S1. Laser power effects

The Raman spectra of GNRs are sensitive to the laser power, especially for the *m*-ANR. For the latter, the D peak strongly changes its shape with increasing laser power (non-reversible trend), so very low laser powers (<< 0.5 mW) need to be used to avoid sample damage. Note that the downshift of the G peak position [Pos(G)] with increasing temperature is in agreement with temperature dependence studies of PAHs and graphene.[1] Using the average value of the G peak dependence on temperature found for PAHs (−0.015 $cm^{-1}/ºC$)[1], one could estimate an increase of up to 270 ºC by increasing the laser power from 0.02 to 0.6 mW.

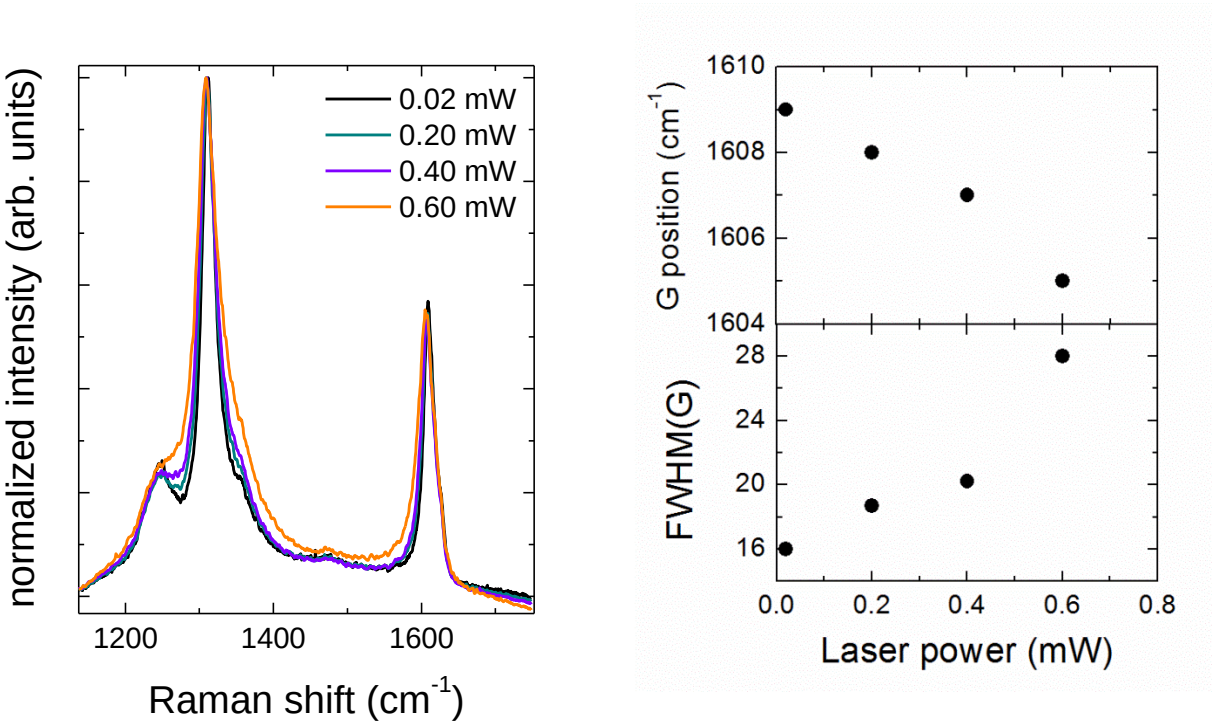

Figure S1 | Raman spectra of m-ANR measured for increasing laser power (left panel). G peak position and FWHM as a function of the laser power (right panel).

S2. Multi-wavelength Raman spectroscopy of GNRs vs defective graphene

Although the Raman spectrum of our GNRs looks, at a first sight, very similar to defective graphene (Figure S2), it shows several unique features that can be used for GNRs identification.

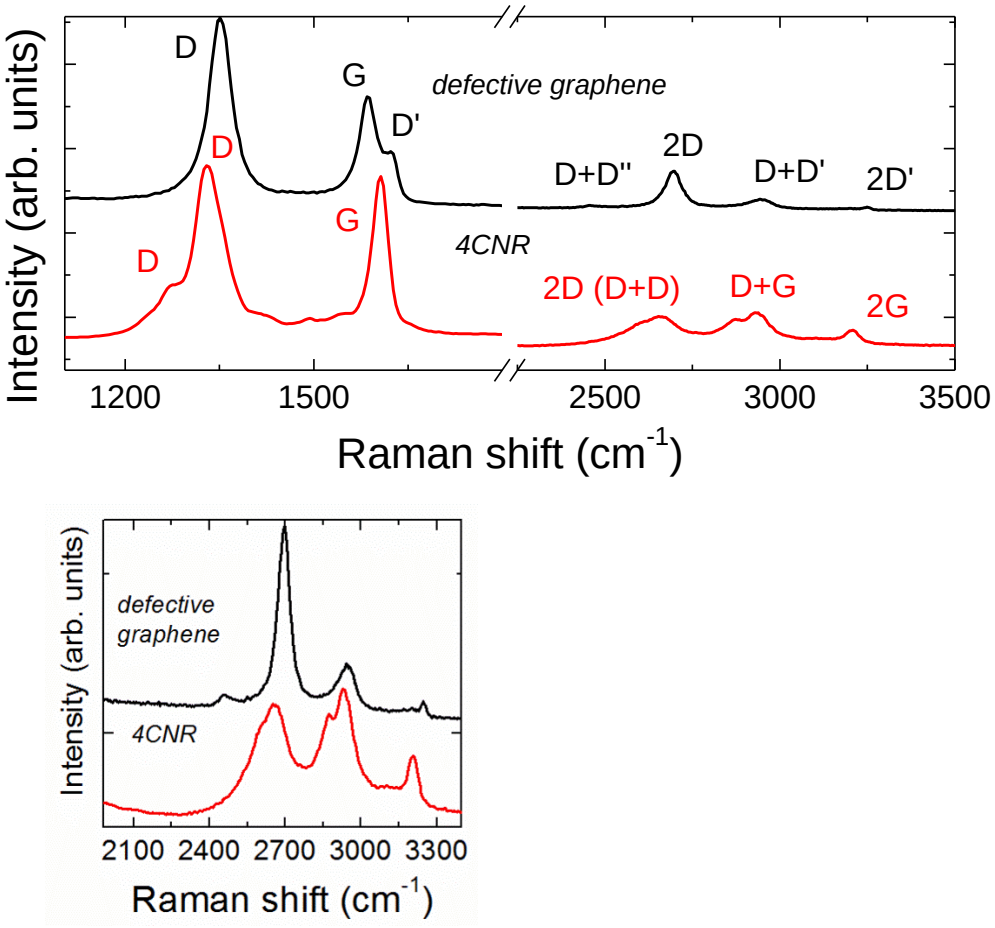

Figure S2 | Raman spectrum of 4CNR cove-shaped ribbon and defective graphene, obtained by using hydrogenation (top panel). Zoom of the high energy region (bottom panel).

In the first order spectrum, the D peak of cove-shape GNRs is typically structured (i.e. composed by at least two components). The G peak is slightly asymmetric and shifted at higher position, as compared to defective graphene. Moving to the high order region, because the D peak is structured, the spectrum shows the overtone and combination modes between the different components of the D peak (called 2D and D+D in Figure S2). The spectrum also shows the D+G and 2G peaks, which are not observed in defective graphene (Figure S2).

Figure S3 | First order and acoustic region of 4CNR (top panels) and 8CNR (bottom panels).

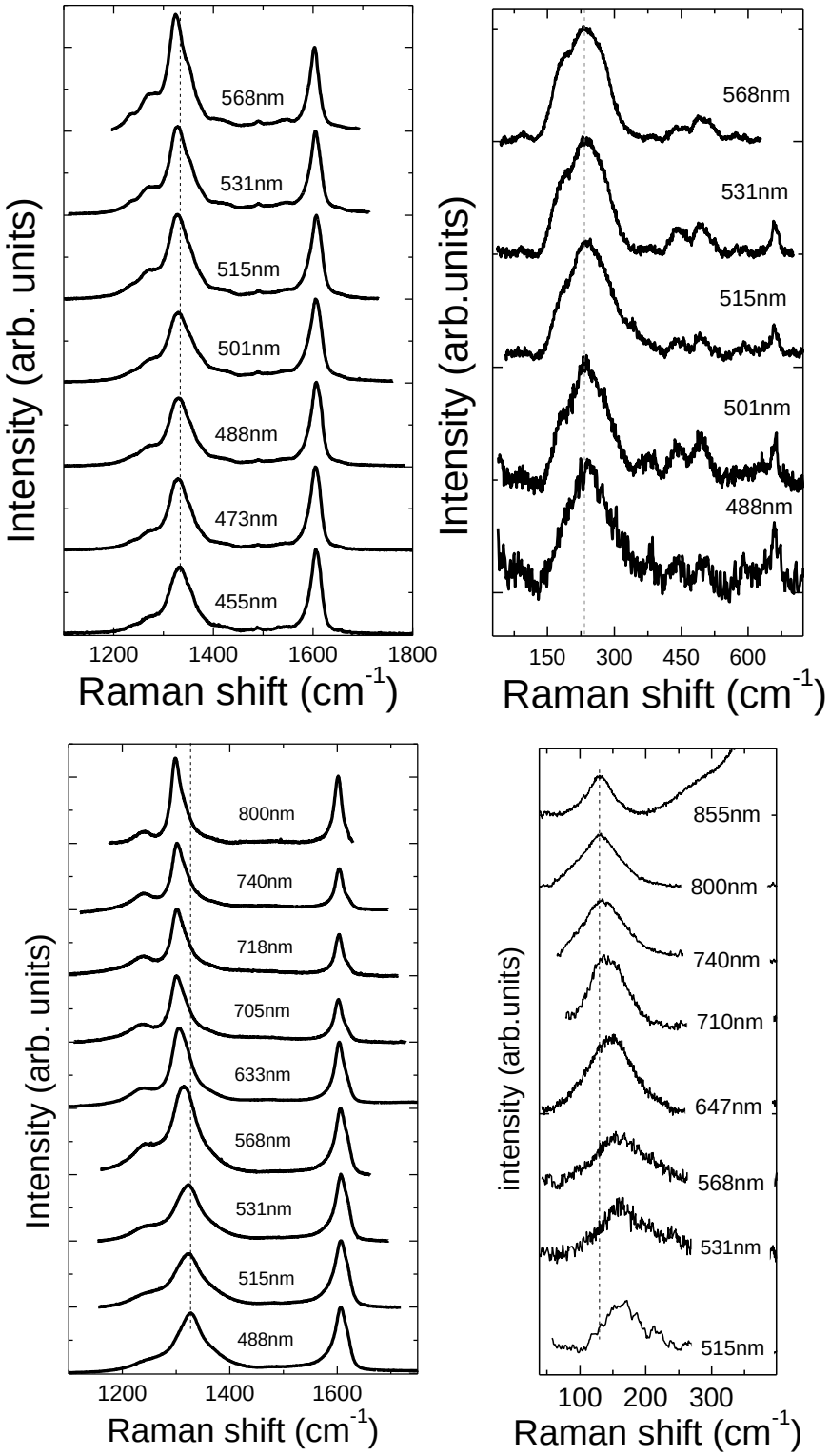

The differences between defective graphene and our GNRs become even more evident when performing multi-wavelength Raman spectroscopy. Figure S3 shows some representative multi-wavelength Raman spectra of 4CNR (top panel) and 8CNR (bottom panel).

In graphene, the D peak is known to change its position with the excitation energy, showing a typical dispersion of ~50 cm^{-1}/eV.[2,3] The D peak dispersion of our GNRs is much smaller: this is evident for the 8CNR ribbons (see main text). Figure S4 shows the D peak dispersion measured in all the ribbons investigated in this work: the D peak dispersion changes from 30 to 10 cm^{-1}/eV, depending on the ribbon type. The RLBM also shows considerable dispersion in some of the ribbons (~30 cm^{-1}/eV for 8CNR), as shown in Figure S3.

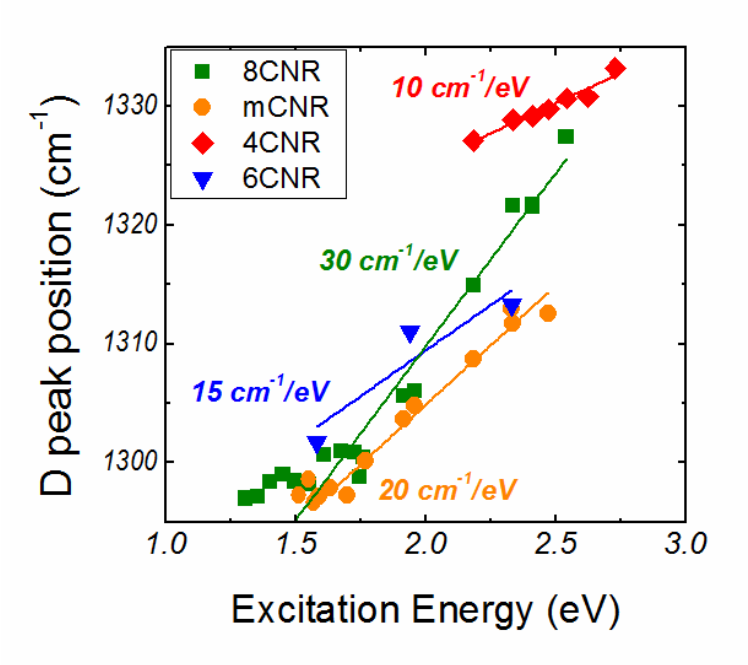

Figure S4 | D peak dispersion for cove-shaped GNRs investigated.

Figure S5 shows a systematic comparison of the D and G peak dispersion of 8CNR with the D and G peak dispersion of defective graphene, with different inter-defect distance (L_D). All the data for defected graphene are taken from Ref. 4.

The effect of an increasing amount of defects on the Raman spectrum of graphene can be described with a phenomenological three-stage model.[4,5] In stage 1), starting from pristine graphene, the Raman spectrum evolves as follows: the D peak appears and the intensity ratio between the D and G peaks [I(D)/I(G)] increases; the D' and D+D' peaks appear; all the peaks broaden and G and D' begin to overlap. In this stage, I(D)/I(G) can be used to estimate the amount of defects.[4,5] At the end of Stage 1), when the distance between defects L_D ~ 4nm, the G and D' peaks are no more distinguishable and I(D)/I(G) starts decreasing. As the number of defects keeps increasing (hence L_D decreases), the Raman spectrum enters Stage 2), showing a marked decrease in Pos(G); I(D)/I(G) sharply decreases towards zero and second-order peaks are no more well defined. Stage 3) describes amorphous materials with increasing sp^3 content. In this stage the Raman spectrum shows an increase in Pos(G), I(D)/I(G) ratio is close to zero and the G peak becomes dispersive with the excitation energy.

Unlike the case of graphene, where the D peak requires a defect for its activation, in PAHs the vibrations corresponding to the D peak are Raman active and do not require any defect to be seen.[6] The energy dependence of both D and G peak uniquely fingerprints the presence of GNRs, being different from both defective graphene and PAHs (Figure S5). Note that we have used $C_{78}H_{26}$ as representative PAH, in view of its D_{2h} symmetry (i.e. elongated geometry, similar to a very short GNRs). All the Raman data related to the $C_{78}H_{26}$ molecule are taken from Ref.1. The Raman spectrum of this molecule is characterized by several D peaks, Figure S5 showing only one of the components. The same applies to the G peak, which has two components in $C_{78}H_{26}$.[1]

Note that the G peak also shows a very small dispersion, Figure S5. A closer look at the G peak shows that the peak is also asymmetric, and that the asymmetry increases for increasing laser energy, Figure S6. Typically, significant disorder and presence of chains in disordered carbon can increase the G peak dispersion.[7] Therefore, the small G dispersion observed here could be related to some disorder (length distribution, imperfect functionalization, etc).

Figure S5 | D peak dispersion of 8CNR, defective graphene with different inter-defect distance and $C_{78}H_{26}$ (top panel). G peak dispersion of 8CNR, defective graphene with different inter-defect distance and $C_{78}H_{26}$ (bottom panel).

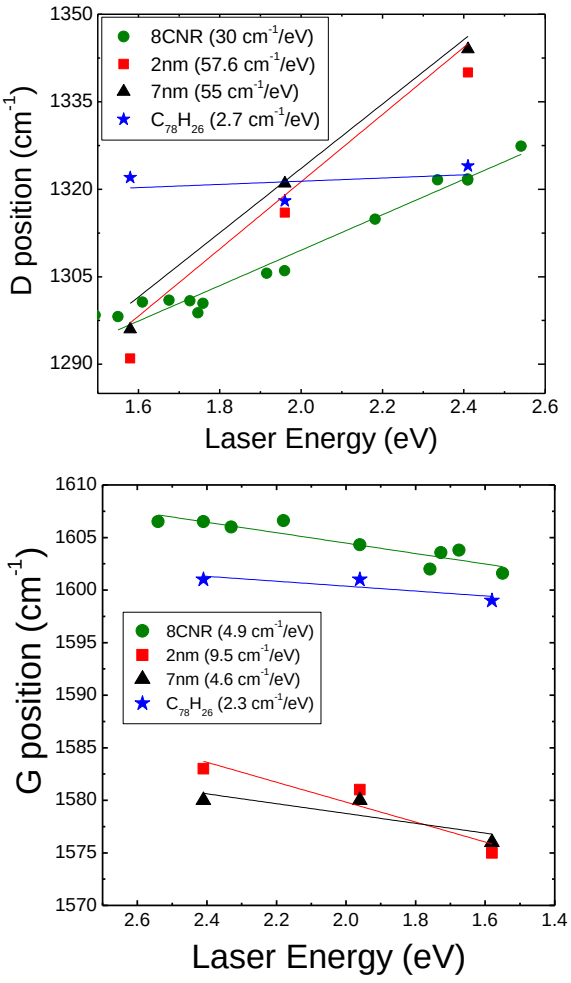

Figure S6 | G peak of 8CNR measured at different excitation wavelengths.

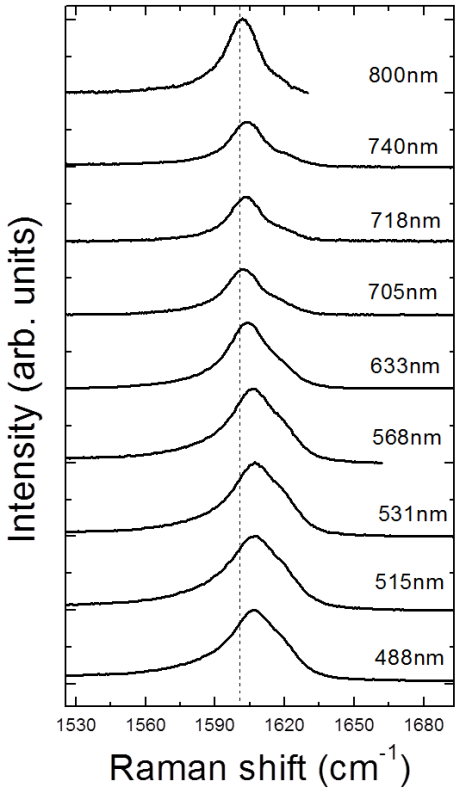

S3. Zone-folding approximation for cove-shaped GNRs.

Similarly to the case of CNTs,[8,9] Pos(RLBM) in armchair and zigzag GNRs is predicted to show an inverse dependence on the GNR width w, which can be formulated as:

$$Pos(RLBM) = \frac{3222\ \text{Å}\,cm^{-1}}{w} \qquad (1)$$

within the zone-folding (ZF) approximation.[10] In the case of cove-shaped graphene GNRs, the width is however not well-defined due to the modulated structure (see Figure S7). We show that the ZF approximation works also for our cove-shaped GNRs, if we define an effective width w_{eff} as the weighted average of the different widths composing the unit cell:

$$w_{eff} = \frac{\sum_{i=1}^{N} w_i a_i}{\sum_{i=1}^{N} a_i}, \qquad (2)$$

where w_i is the width of the i-th component and a_i is its multiplicity (i.e. number of GNR unit cells with the same width, see Figure S7). The comparison of such a ZF approach with DFPT simulations is reported in Figure 3b of the main text, while Figure S7b shows the absolute difference of Pos(RLBM) between DFPT calculations and ZF results, which are obtained by setting the w in Eqn. 1 equal to the minimal (w_{min}), maximal (w_{max}), or effective width (w_{eff}, Eqn. 2) of the GNR. As discussed in the main text, for smaller GNR widths (i.e. 4- and 6CNR) we notice a larger deviation of the RLBM frequencies obtained from ZF from DFPT, since in this range of widths/wave-vectors the ZF does not hold anymore (i.e. the RLBM cannot be folded on the LA branch of graphene).[10]

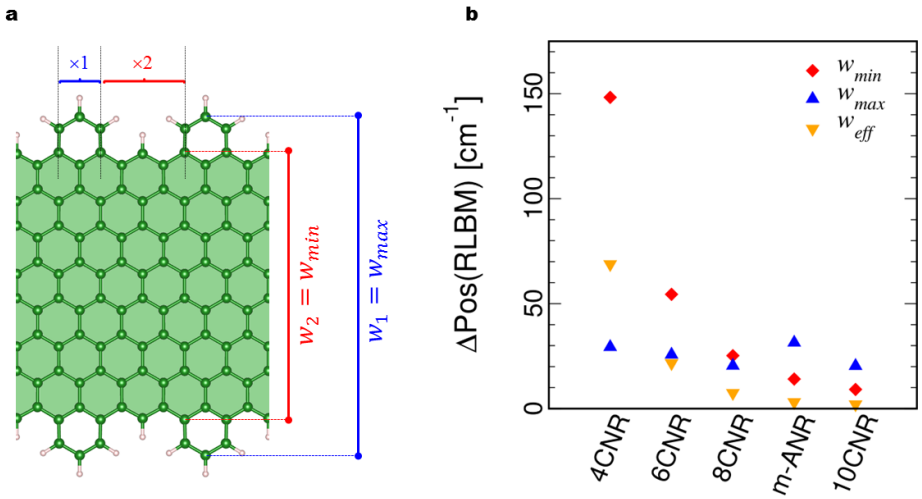

Figure S7 | Defining an effective width for the ZF approximation. a, Ball-and-stick model of the 8CNR, where the width and multiplicity of the different components is highlighted. **b,** Comparison of DFPT and ZF results for Pos(RLBM), as obtained by using the minimal (w_{min}), maximal (w_{max}), or effective width (w_{eff}). ΔPos(RLBM) is the absolute difference between DFPT and ZF Pos(RLBM).

S4. D- and G-peak dispersions from DFPT.

Figure S8 reports the phonon dispersion as a function of **q** for the smaller GNR investigated here, i.e. the 4CNR, in the region around the D and G mode (indicated by red arrows). The system is fully H-passivated. This comparison shows that the branch giving rise to the D peak is much more dispersive than the one giving rise to the G peak.

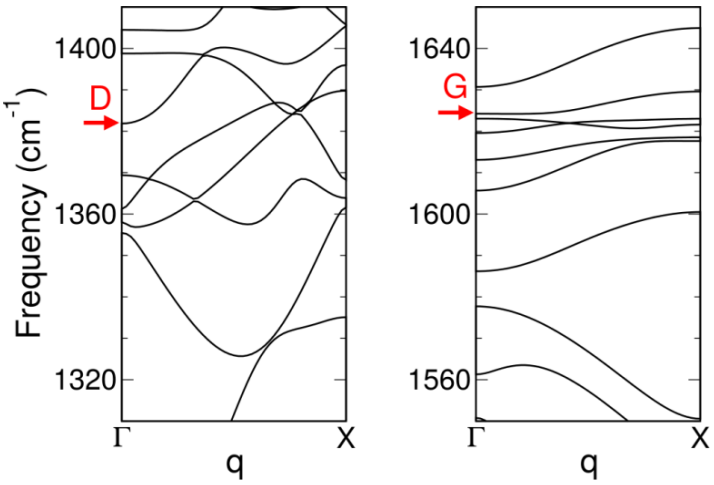

Figure S8 | Phonon dispersion for 4CNR in the D-peak (left panel) and G-peak (right panel) energy region.

S5. Simulated Raman spectra for cove-shaped GNRs: chirality and chain effects.

Chirality. As shown in Figure 1 of the main text, m-ANR and 8CNR have the same nominal width, but different chirality. Their RLBM frequencies calculated within DFPT differ by ~10 cm^{-1} (green and orange arrows in the bottom panel of Figure S9). Moreover, the LA mode (~125 cm^{-1}) becomes Raman active for the m-ANR, while it is inactive for the 8CNR.

Chain effects. The top and middle panels of Figure S9 report the Raman spectra for 4- and 6-CNR. In presence of alkyl side chains, the RLBM is usually found at lower frequencies (even though mixed modes partially bearing a breathing character can be observed at higher frequencies). Moreover, the relaxation of the system symmetry mixes longitudinal (L), transverse (T) and normal (Z) modes, activating modes otherwise forbidden. Note also that these features depend on both the chain length and the GNR width. For instance, the -C_4H_9 side chain already gives rise to different sub-peaks for the 4CNR, while for the 8CNR we need a longer chain to see this effect (see e.g. the case of C_8H_{17}, Figure 3d of the main text).

In the case of 6CNR, we also compare the spectra for different locations of the side chains, i.e. substituted at the outer positions on the fused benzo rings (e), or at the inner position inside the cove-type edge (c), as in real samples. In the first case, structures and spectra are similar to those of the other GNRs; in the latter, the GNR backbone is distorted due to the steric hindrance of the –H and –C_4H_9 terminations, modifying frequency and shape of both D and G peaks.

To further appreciate the sensitivity of the low-energy modes on the chain conformation, we have also compared the spectra obtained by considering in-plane (ip) and out-of-plane (oop) configurations of the side chains [i.e., the C=C bonds of the alkyl chains are either lying in-plane with respect to the GNR backbone (ip), or lying in a plane perpendicular to the GNR backbone and to the GNR main axis (oop)], as shown in Figure S10.

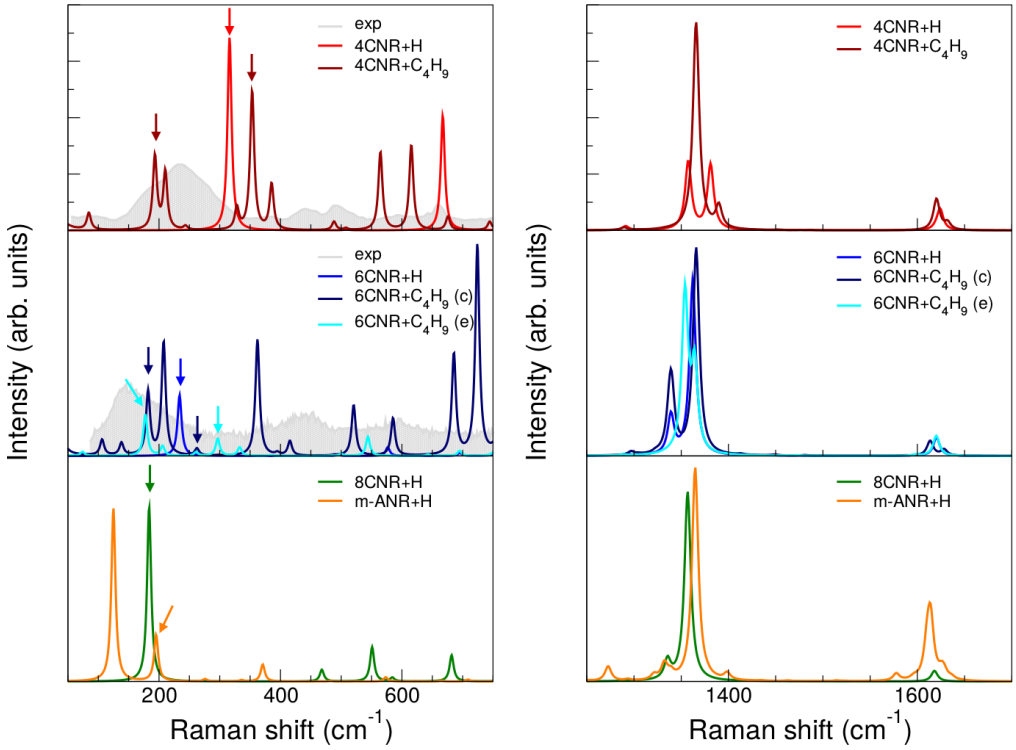

Figure S9 | Simulated Raman spectra for 4CNR, 6CNR and m-ANR. Acoustic **(left)** and optical **(right)** region of the Raman spectrum for the GNRs shown in Figure 1 of the main text. In the middle panels, we compare the spectra for alkyl chains attached in cove (c) or edge (e) position in the case of the 6CNR. In the bottom panels, the m-ANR is compared with the 8CNR (both fully hydrogenated). Vertical arrows indicate the RLBMs.

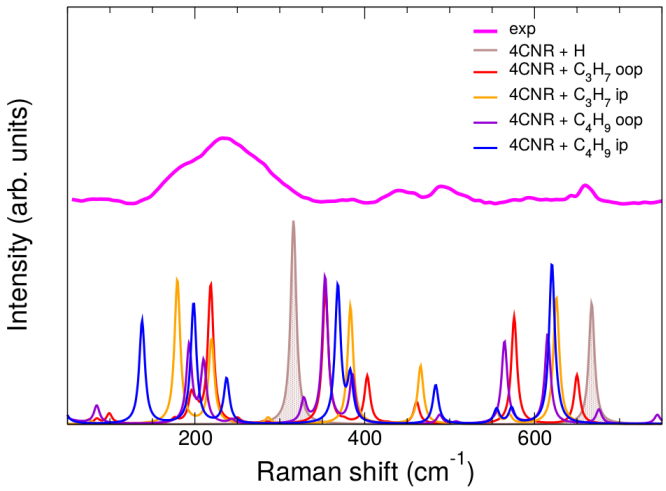

Figure S10 | Simulated Raman spectra for functionalized 4CNR. We compare the low-energy spectral region of 4CNR functionalized with side chains placed in-plane (ip) or out-of-plane (oop) with respect to the GNR backbone. Slightly different lengths are also considered.

References

(1) Maghsoumi, A.; Brambilla, L.; Castiglioni, C.; Müllen, K.; Tommasini, M. *J. Raman Spectrosc.* **2015**, *46* (9), 757–764.

(2) Ferrari, A. C.; Meyer, J. C.; Scardaci, V.; Casiraghi, C.; Lazzeri, M.; Mauri, F.; Piscanec, S.; Jiang, D.; Novoselov, K. S.; Roth, S.; Geim, A. K. *Phys. Rev. Lett.* **2006**, *97* (18), 187401.

(3) Casiraghi, C.; Hartschuh, A.; Qian, H.; Piscanec, S.; Georgi, C.; Fasoli, A.; Novoselov, K. S.; Basko, D. M.; Ferrari, A. C. *Nano Lett.* **2009**, *9* (4), 1433–1441.

(4) Cançado, L. G.; Jorio, A.; Ferreira, E. H. M.; Stavale, F.; Achete, C. A.; Capaz, R. B.; Moutinho, M. V. O.; Lombardo, A.; Kulmala, T. S.; Ferrari, A. C. *Nano Lett.* **2011**, *11* (8), 3190–3196.

(5) Bruna, M.; Ott, A. K.; Ijäs, M.; Yoon, D.; Sassi, U.; Ferrari, A. C. *ACS Nano* **2014**, *8* (7), 7432–7441.

(6) Castiglioni, C.; Tommasini, M.; Zerbi, G. *Phil. Trans. R. Soc. Lond. A* **2004**, *362* (1824), 2425–2459.

(7) Ferrari, A. C.; Robertson, J. *Phys. Rev. B* **2001**, *64* (7), 075414.

(8) Saito, R.; Dresselhaus, G.; Dresselhaus, M. S. *Physical Properties of Carbon Nanotubes*; Imperial College Press, London, 1998.

(9) Reich, S.; Thomsen, C.; Maultzsch, J. *Carbon Nanotubes: Basic Concepts and Physical Properties*; Wiley-VCH Verlag GmbH, 2004.

(10) Gillen, R.; Mohr, M.; Maultzsch, J. *Phys. Rev. B* **2010**, *81* (20), 205426.